List of Supplementary material

Supplementary Methods

Supplementary Tables

Supplementary Figures

Supplemental References

Supplementary Movie

Supplementary Movie S1 (in mp4 or pdf format, note that you must view the mp4 format online). The binding model of binding SRP68 by SRP72. To bind SRP68, SRP72 homodimer disassociates, its C-terminal cap undergoes pronounced conformational changes and forms a SRP68/SRP72 heterodimer.

Supplementary Validation Reports

Two PDB validation reports for apo-SRP72 and SRP68-SRP72 complex

Supplementary Methods

Structure determination and refinement

The heavy atom position in the Hg-derived SRP68/72 crystal of space group $P6_322$ was determined using program SHELEX C (Sheldrick, 2008) with single-wavelength anomalous diffraction (SAD). One initial Hg site was found and the phases were generated. The crude partial model with 10 helices in 162 residues was built by program SHELEX E (Sheldrick, 2008) and figure of merit reached 0.70. The model was further built in program AUTOBUILD (Adams et al., 2010) followed by COOT (Emsley et al., 2010) and refined using REFMAC5 (Murshudov et al., 2011) in iterative cycles. Then the native data was used and complex structure was refined finally to 1.70 Å with an R_{work} of 16.3% and an R_{free} of 18.9%. The apo-SRP72 structure was solved by the MolRep program in the CCP4 suite (Winn et al., 2011) using the SRP72 structure from the determined SRP68/72 complex as a model after extensive trials of deleting helices. The structure was refined to 2.91Å in space group $P2_12_12_1$ with an R_{work} of 23.1% and an R_{free} of 26.6%. Coordinates and structure factors have been deposited in the Protein Data Bank under accession code 5WRW and 5WRV, for apo-SRP72 and SRP68/72 complex, respectively. All figures in this article displaying molecular structure were made using PYMOL (Schrödinger, 2010).

Size-Exclusion Chromatography and Analytical Ultracentrifugation

Size-exclusion chromatography experiments for the purified recombinant SRP68/72 and SRP72 were applied to sieve columns (Superdex-75 or Superdex-200, GE Healthcare) equilibrated with buffers containing 20 mM Tris-HCl pH 8.0 and 500 mM NaCl. Peak fractions were collected and visualized by SDS-PAGE followed by Coomassie Bright Blue staining.

Sedimentation velocity (SV) analytical ultracentrifugation experiments were performed in a Beckman/Coulter XL-I analytical ultracentrifuge using double-sector or six-channel centerpieces and sapphire windows. An additional protein purification step applied to size-exclusion chromatography in buffer containing 20 mM Tris pH 8.0, 150 mM NaCl was performed before experiments. SV experiments were conducted at 42,000 rpm and 20 ℃ using interference detection and double-sector cells loaded at approximate 0.1 mM for SRP72. The buffer composition (density and viscosity) and protein partial specific volume (V-bar) were obtained using the program SEDNTERP and SV data were analyzed using the SEDFIT programs (Schuck, 2000, 2003).

CD Analysis

The CD spectra of the proteins were measured at the 4B8 beamline in the BSRF. Spectra were collected at 1 nm intervals over the wavelength ranging from 260 to 180 nm in a 0.005 cm optical path length at 25 ℃. A pure solution baseline collected with the same cell was subtracted, and all spectra data were processed using the CD tool software (Lees et al., 2004). Protein samples were prepared at a concentration of about 1 mg/ml. The machine unit (mdeg) was converted into the per residue molar absorption unit, delta epsilon (Δε) in M/cm, by normalization with respect to polypeptide concentration and path length.

Small-angle X-ray scattering

Small angle X-ray scattering (SAXS) measurements of the recombinant apo-SRP72 in a buffer containing 20 mM Tris-HCl pH 8.0 and 500 mM NaCl, were performed at the beamline BL19U2 of the SSRF using previously published methods (Hu et al., 2015; Zhang et al., 2012). Briefly, all proteins were subjected to size exclusion chromatography in a buffer containing 20 mM Tris-HCl pH 8.0 and 500 mM NaCl. Various concentrations of protein (40 μl) were used, and the data were collected at 1.03 Å with a distance of 1 m from the detector. Individual data were processed by RAW (Nielsen et al., 2009). The scattering data from the buffer alone was measured before and after each sample measurement, and the average of the scattering data was used for background subtraction. The theoretical scattering curves from the possible configurations of all proteins were fitted to the experimental scattering curve using the Minimal Ensemble Search (MES) algorithm (Pelikan et al., 2009).

GST-mediated pull-down assay

Flag-SRP68, His-SRP72, GST-SRP68 and mutants were purified using appropriate affinity columns. 200 μg GST-SRP68 mutants was immobilized on glutathione sepharose resin (GE Healthcare) and incubated with His-SRP72 at 4 ℃ for 1 h in a buffer of 20 mM Tris-HCl pH 8.0, 500 mM NaCl, 2 mM β-ME, 1 mM PMSF and 10% glycerol. The resin was extensively rinsed with buffer containing 20 mM Tris-HCl pH 8.0, 500 mM NaCl, 2 mM DTT and 5 mM β-ME to remove unbound or non-specific bound proteins 4 times. Proteins left on the beads were boiled in protein loading buffer, separated by SDS-PAGE and analyzed by Western blotting.

Western blotting

Cells were lysed in 2 × SDS sample buffer or lysis buffer (20 mM Tris-HCl pH 8.0, 200 mM NaCl, 1% Triton X-100, 1 mM DTT, 1 × complete protease inhibitor cocktail, 10% glycerol). The protein samples were resolved by SDS-PAGE and transferred onto a polyvinylidene difluoride membrane, which was blocked in 5% skim milk and probed with the anti-His, anti-GST and anti-Flag antibodies.

Microscale thermophoresis (MST)

The binding affinity of wild-type and mutated GST-SRP68 to SRP72 was measured using MST. Wild-type and mutated GST-SRP68 was labeled with fluorescent dye NT-647 (Cysteine Reactive) according to the manufacturer's protocol. A series of wild-type and mutated SRP72 solutions with different concentrations was prepared by consecutive twofold dilutions in buffer containing 20 mM HEPES pH 8.0, 650 mM NaCl, and 0.05% Tween-20 from the highest concentration of 40 μM. The labeled 0.5 μM wild-type and mutated GST-SRP68 protein was mixed with wild-type and mutated SRP72 proteins prepared at a volume ratio of 1:1. The samples were loaded into silica capillaries after incubation at room temperature. After 30 min, the measurements were performed at 25 ℃ by using 40% LED power and 40% MST power. Data analyses were performed by using the NTAnalysis software (NanoTemper Technologies).

Supplementary Table S1. Summary of residues where cancer-associated mutations occur in SRP72 and SRP68.

SRP72 variants	Diseases	**SRP68 variants**	Diseases
V9*	Colon adenocarcinoma Stomach carcinoma Colorectal cancer (Mouradov et al., 2014) (Kim et al., 2014) (Giannakis et al., 2014)	F590L	Colon adenocarcinoma (Cancer Genome Atlas Network, 2012)
A13P	Esophageal Cancer	K606E	Colorectal cancer
N19K	Esophageal squamous cell carcinoma (Zhang et al., 2015)	Q609H	Uterine corpus endometrioid carcinoma
Y21C	Malignant melanoma (Shain et al., 2015)		
N41K	Kidney renal clear cell carcinoma		
D44H	Lung squamous cell carcinoma		
D44E	Lund adenocarcinoma (Imielinski et al., 2012)		
V45I	Gastric adenocarcinoma		
V53A	Large intestine carcinoma (Giannakis et al., 2014)		
V53I	Gastric adenocarcinoma		
N58*	Papillary renal cell carcinoma (Durinck et al., 2015)		
S81T	Malignant melanoma (Shain et al., 2015)		
Y86C	Liver cancer Hepatocellular carcinoma (Guichard et al., 2012) (Schulze et al., 2015)		
E88Q	Squamous cell carcinoma (Sawada et al., 2016)		
R121H	Brain lower grade glioma		
R137Q	Uterine corpus endometrioid carcinoma		
S139Y	Uterine corpus endometrioid carcinoma		

The diseases are searched in the website of COSMIC (Catalogue of Somatic Mutations in Cancer). These residues in red are also shown in the Figure 5.

Supplementary Table S2. The experimental Small-angle X-ray scattering (SAXS) results of apo-SRP72$^{1\text{-}163}$ at variation concentration. R_g, radius of gyration; Dmax, maximum linear dimension. MW_{Porod}, molecular mass.

Concentration (mg/ml)	Data Quality	R_g (Å)	$D_{\max}$ (Å)	MW_{Porod} (kDa)
2.0	75%	30.5 ± 2.6	101	36
5.0	81%	30.5 ± 1.3	130	40
10.0	80%	32.1 ± 0.9	137	43
15.0	83%	33.2 ± 0.9	154	46
20.0	80%	33.4 ± 0.9	149	47
25.0	87%	35.0 ± 1.0	157	50

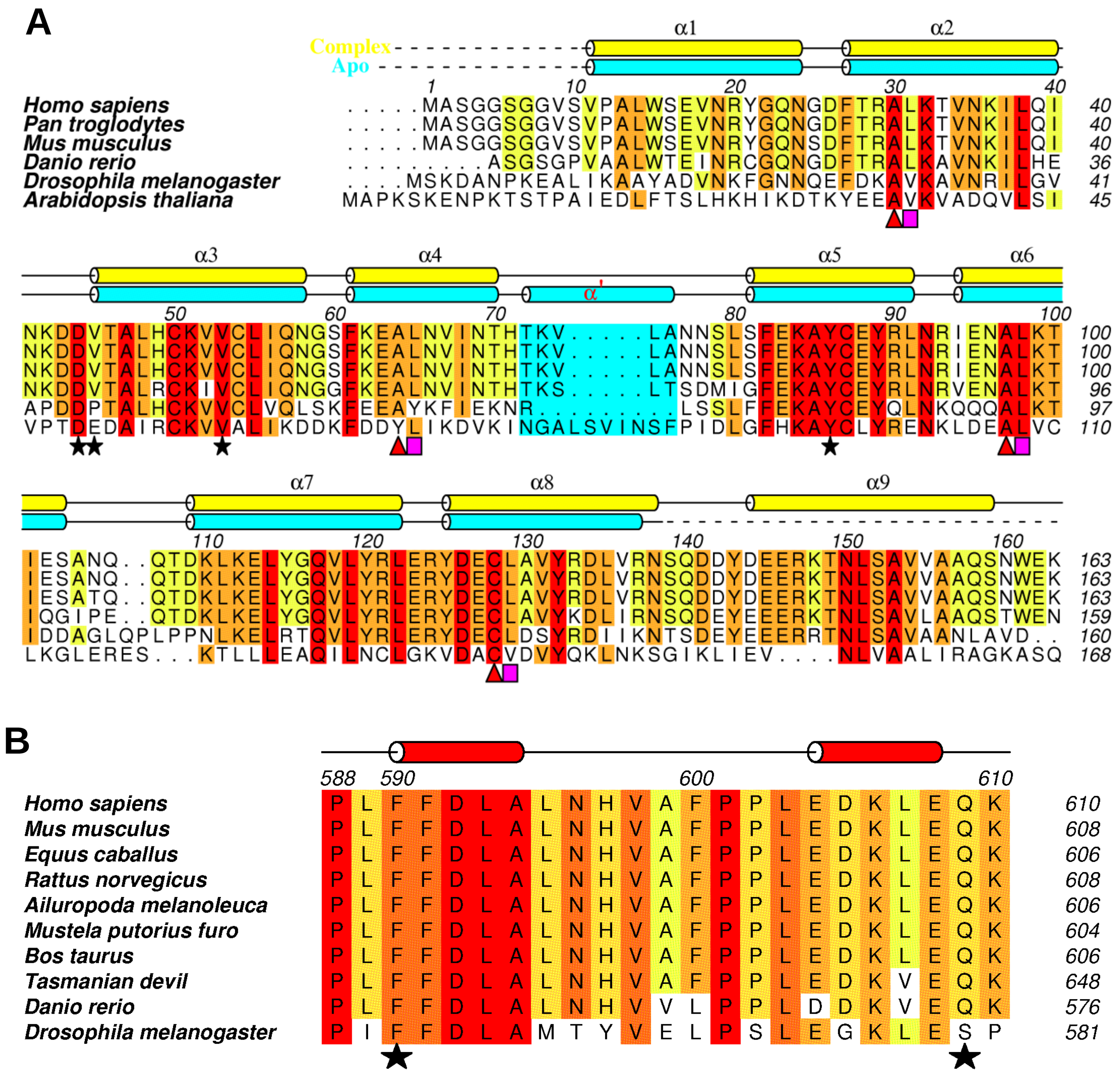

Supplementary Figure S1. Sequence alignment of SRP68 and SRP72 from different species.

Sequences of representative eukaryotes are shown together with the secondary structure of human SRP68 and SRP72. Secondary structural elements (cylinders for helices) of SRP68-free and SRP68-bound human SRP72 structures, and SRP68 are calculated by DSSP and colored cyan, yellow and red, respectively. The above numbers indicate residues for human SRP68 and SRP72. Black stars indicate residues included in mutational analyses (see Fig. 5; Supplemental Table 1).

(A). The conserved residues from TPR alignment (Fig. 1E) are colored in red triangles and magnetic square boxes, respectively. Interestingly, the α9 found in the SRP68-bound structure is disordered in the structure of human apo-SRP72 (dashed line). On the contrary, α' is only found in apo-SRP72 and not conserved. The sequences used are from: SRP72, signal recognition particle 72. *Homo sapiens*

(GenBank accession # - NP_008878.3); *Pan troglodytes* (JAA21875.1); *Mus musculus* (NP_079967.1); *Danio rerio* (AAH67641.1); *Drosophila melanogaster* (NP_650898.1); *Arabidopsis thaliana* (AEE34676.1).

(B). SRP68, signal recognition particle 68. *Homo sapiens* (Q9UHB9.2); *Mus musculus* (NP_079967.1); *Equus caballus* (XP_001915704.1); *Rattus norvegicus* (NP_001102310.1); *Ailuropoda melanoleuca* (XP_002919905.1); *Mustela putorius furo* (XP_004748919.1); *Bos taurus* (AAI50017.1); *Tasmanian devil* (XP_003768559.1); *Danio rerio* (NP_001005401.2); *Drosophila melanogaster* (NP_648273.1). The ALINE program (Bond and Schuttelkopf, 2009) was used to prepare the figure.

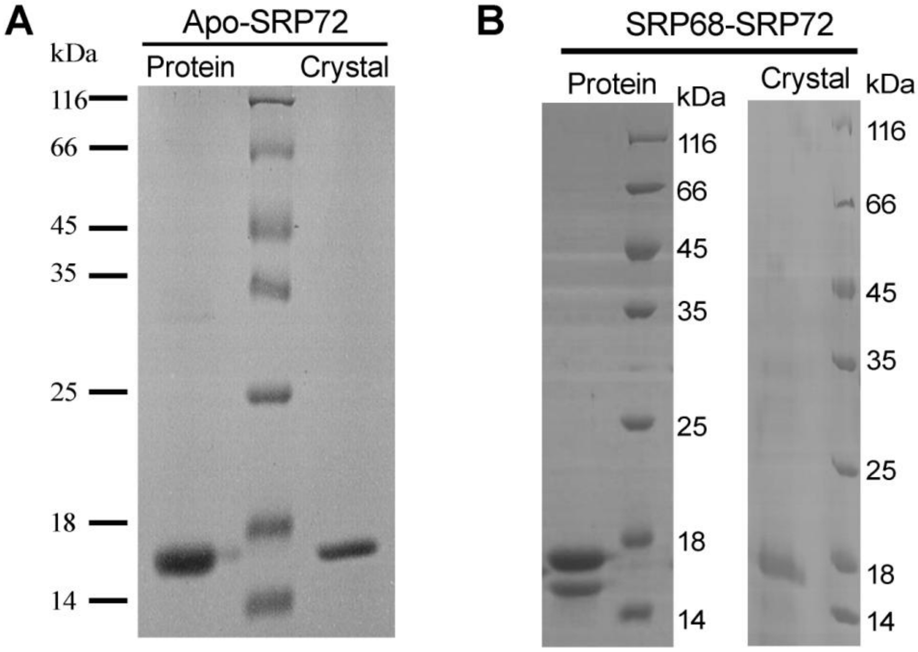

Supplementary Figure S2. The proteins before and after crystallization.

(A). Apo-SRP72. Both proteins were equal in size (~18.5 kDa), implying that the last helix α9 missed in the apo-SRP72 structure was due to its flexibility.

(B). SRP68-SRP72 complex. The figures showed that SRP68 (~11.8 kDa) degraded during the crystallization process. The proteins purified from *E. coli* and the crystals were resolved by SDS-PAGE and visualized by Coomassie blue staining.

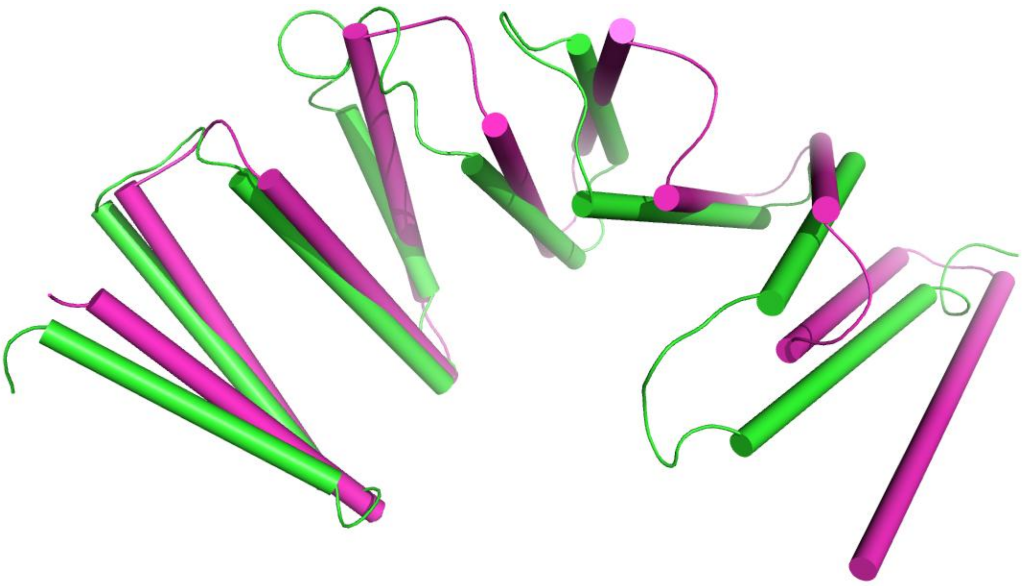

Supplementary Figure S3. Structural superimposition of SRP72 onto magnetosome protein MamA (PDB ID: 3vty) (Zeytuni et al., 2011; Zeytuni and Zarivach, 2012) with a RMSD of 3.1.

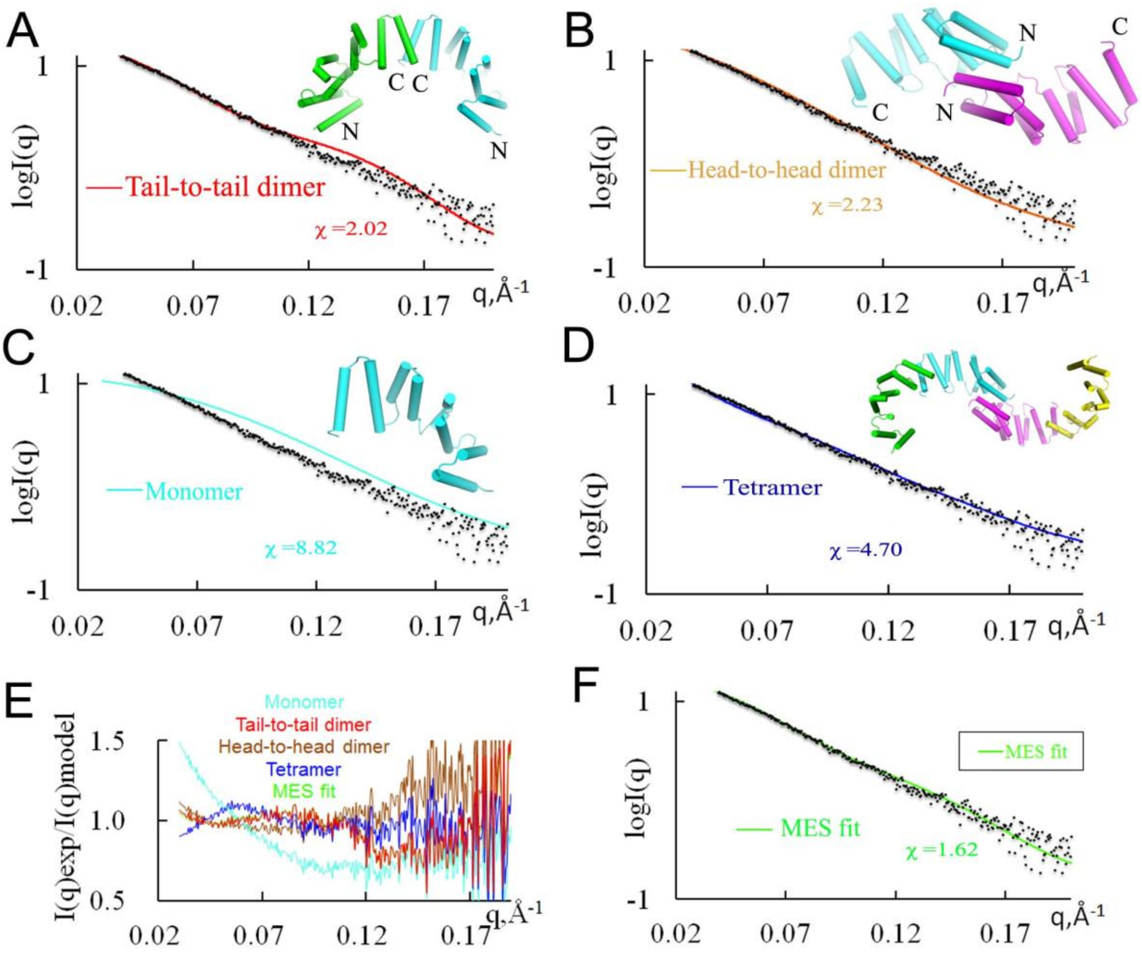

Supplementary Figure S4. Comparison of SAXS experimental data and calculated scattering profiles for various apo-SRP72 models at 2 mg/ml concentration.

Experimental data are represented in black dots. The theoretical scattering curves of (**A**) tail-to-tail dimer (red), (**B**) head-to-head dimer (orange), (**C**) monomer (cyan), (**D**) tetramer (navy) and (**F**) the assembly from MES fit (green) are shown. (**E**) Residuals of five models calculated as I(q) experimental/I(q)model.

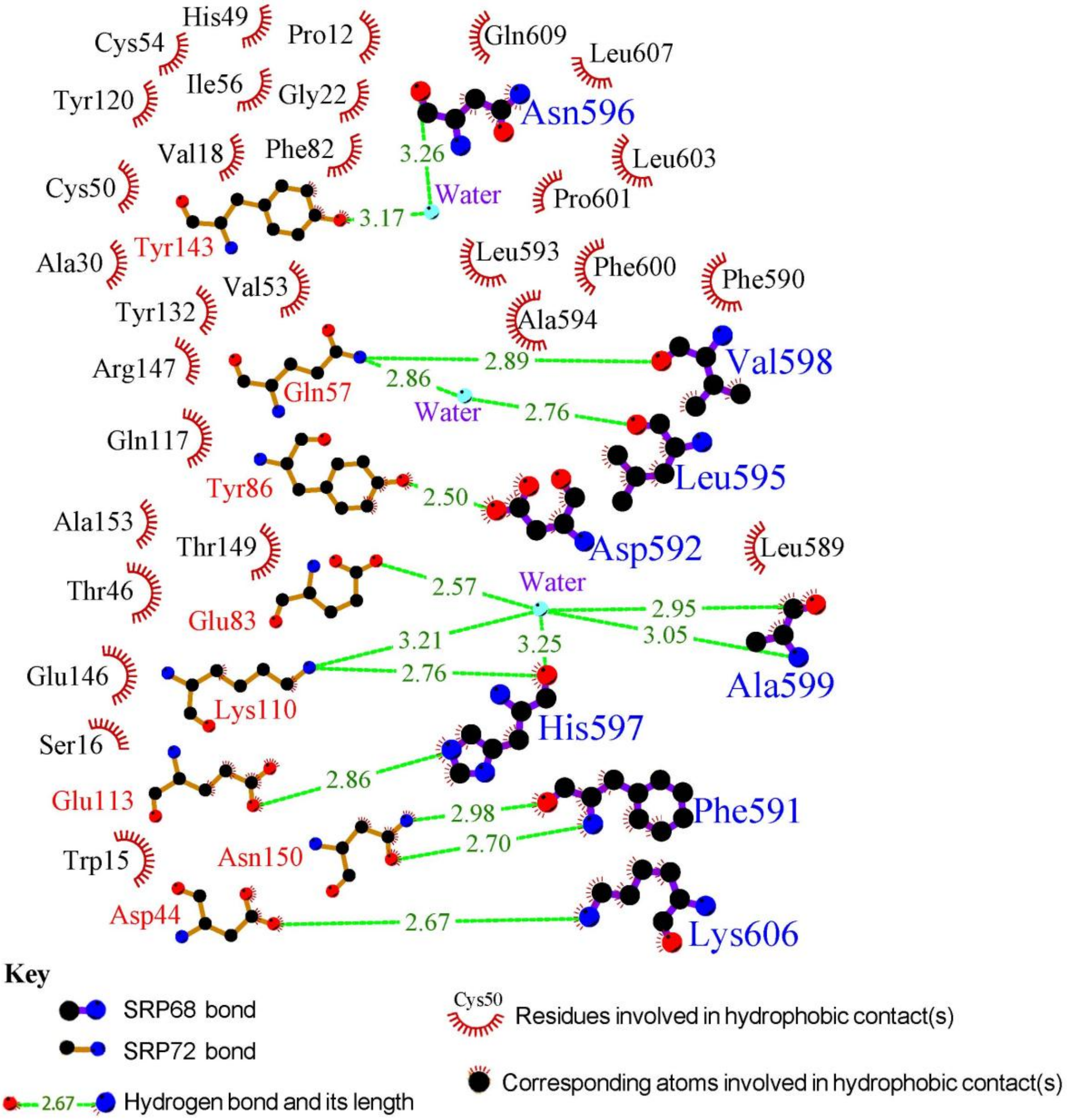

Supplementary Figure S5. Detailed description of the interactions between SRP72 and SRP68 in the complex.

Ligplot (Imielinski et al., 2012) was used to generate the interactions. Hemispheres represent hydrophobic interactions whereas lines represent polar interactions. The residues from SRP72 and SRP68 are shown in left and right, respectively. All the residues involved in the hydrophobic interaction are shown in black. For hydrophilic interaction, the residues from SRP72 and SRP68 are shown in red and blue, respectively.

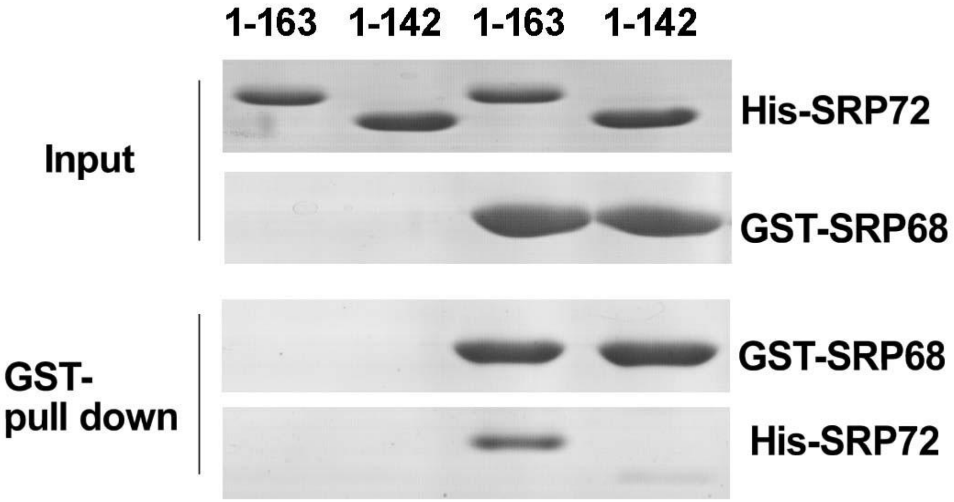

Supplementary Figure S6. The extra helix α9 is responsible for the binding of SRP72 to SRP68.

Binding of the α9 (cap) deletion mutant of SRP72 (fragment 1-142) to SRP68 is significantly reduced. Purified GST-tagged SRP68 was used for GST pull-down of purified His-SRP72 proteins, and analyzed by SDS-PAGE and commassie blue staining.

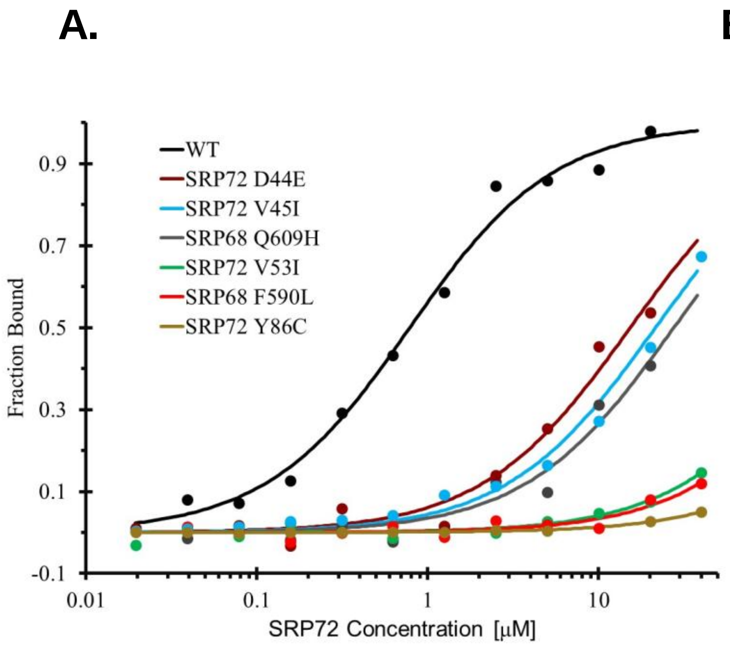

B.

Labeled SRP68	SRP72	K_D (μM)
WT	WT	0.73
WT	D44E	15.28
WT	V45I	21.47
WT	V53I	232.8
WT	Y86C	741.45
F590L	WT	286.52
Q609H	WT	27.52

Supplementary Figure S7. The MST binding data of interactions between SRP68 and SRP72 variants

(A). Microscale thermophoresis measurements of the interactions between the wild-type SRP68 and wild-type SRP72 (black), wild-type SRP68 and SRP72 D44E (peony), wild-type SRP68 and SRP72 V45I (blue), SRP68 Q609H and wild-type SRP72 (gray), wild-type SRP68 and SRP72 V53I (green), SRP68 F590L and wild-type SRP72 (red), and wild-type SRP68 and SRP72 Y86C (brown) are shown.

(B). The dissociation constants (K_D) of different SRP68 toward SRP72 determined by MST.

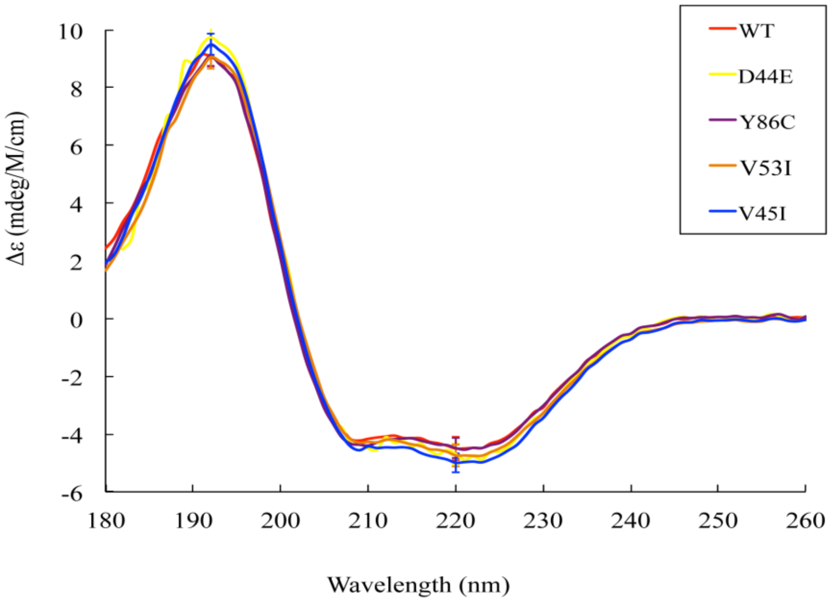

Supplementary Figure S8. The circular dichroism data of wild-type SRP72 and various mutants. The spectral shapes of wild-type and mutated SRP72 were almost identical, demonstrating that the secondary structures of SRP72 mutants were similar to those in the wild-type SRP72.

Supplementary References:

Adams, P.D., Afonine, P.V., Bunkoczi, G., et al. (2010). PHENIX: a comprehensive Python-based system for macromolecular structure solution. Acta Crystallogr. D Biol. Crystallogr. *66*, 213-221.

Bond, C.S., and Schuttelkopf, A.W. (2009). ALINE: a WYSIWYG protein-sequence alignment editor for publication-quality alignments. Acta Crystallogr. D Biol. Crystallogr. *65*, 510-512.

Cancer Genome Atlas Network (2012). Comprehensive molecular characterization of human colon and rectal cancer. Nature *487*, 330-337.

Durinck, S., Stawiski, E.W., Pavia-Jimenez, A., et al. (2015). Spectrum of diverse genomic alterations define non-clear cell renal carcinoma subtypes. Nat. Genet *47*, 13-21.

Emsley, P., Lohkamp, B., Scott, W.G., et al. (2010). Features and development of Coot. Acta Crystallogr. D Biol. Crystallogr. *66*, 486-501.

Giannakis, M., Hodis, E., Jasmine Mu, X., et al. (2014). RNF43 is frequently mutated in colorectal and endometrial cancers. Nat. Genet *46*, 1264-1266.

Guichard, C.c., Amaddeo, G., Imbeaud, S., et al. (2012). Integrated analysis of somatic mutations and focal copy-number changes identifies key genes and pathways in hepatocellular carcinoma. Nat. Genet *44*, 694-698.

Hu, Y., Chen, Z., Fu, Y., et al. (2015). The amino-terminal structure of human fragile X mental retardation protein obtained using precipitant-immobilized imprinted polymers. Nat Commun. *6*, 6634.

Imielinski, M., Berger, A.H., Hammerman, P.S., et al. (2012). Mapping the hallmarks of lung adenocarcinoma with massively parallel sequencing. Cell *150*, 1107-1120.

Kim, T.M., Jung, S.H., Kim, M.S., et al. (2014). The mutational burdens and evolutionary ages of early gastric cancers are comparable to those of advanced gastric cancers. J Pathol. *234*, 365-374.

Lees, J.G., Smith, B.R., Wien, F., et al. (2004). CDtool-an integrated software package for circular dichroism spectroscopic data processing, analysis, and archiving. Anal. Biochem. *332*, 285-289.

Mouradov, D., Sloggett, C., Jorissen, R.N., et al. (2014). Colorectal cancer cell lines are representative models of the main molecular subtypes of primary cancer. Cancer Res. *74*, 3238-3247.

Murshudov, G.N., Skubak, P., Lebedev, A.A., et al. (2011). REFMAC5 for the refinement of macromolecular crystal structures. Acta Crystallogr. D Biol. Crystallogr. *67*, 355-367.

Nielsen, S.S., Toft, K.N., Snakenborg, D., et al. (2009). BioXTAS RAW, a software program for high-throughput automated small-angle X-ray scattering data reduction and preliminary analysis. J. Appl. Crystallogr. *42*, 959-964.

Pelikan, M., Hura, G.L., and Hammel, M. (2009). Structure and flexibility within proteins as identified through small angle X-ray scattering. Gen. Physiol. Biophys. *28*, 174-189.

Sawada, G., Niida, A., Uchi, R., et al. (2016). Genomic Landscape of Esophageal Squamous Cell Carcinoma in a Japanese Population. Gastroenterology *150*, 1171-11782.

Schrödinger, L. (2010). The PyMOL Molecular Graphics System,Version 1.3.

Schuck, P. (2000). Size-distribution analysis of macromolecules by sedimentation velocity ultracentrifugation and lamm equation modeling. Biophys. J. *78*, 1606-1619.

Schuck, P. (2003). On the analysis of protein self-association by sedimentation velocity analytical ultracentrifugation. Anal. Biochem. *320*, 104-124.

Schulze, K., Imbeaud, S., Letouzé, E., et al. (2015). Exome sequencing of hepatocellular carcinomas identifies new mutational signatures and potential therapeutic targets. Nat. Genet *47*, 505-511.

Shain, A.H., Garrido, M., Botton, T., et al. (2015). Exome sequencing of desmoplastic melanoma identifies recurrent NFKBIE promoter mutations and diverse activating mutations in the MAPK pathway. Nat. Genet *47*, 1194-1199.

Sheldrick, G.M. (2008). A short history of SHELX. Acta Crystallogr. A. *64*, 112-122.

Winn, M.D., Ballard, C.C., Cowtan, K.D., et al. (2011). Overview of the CCP4 suite and current developments. Acta Crystallogr. D Biol. Crystallogr. *67*, 235-242.

Zeytuni, N., Ozyamak, E., Ben-Harush, K., et al. (2011). Self-recognition mechanism of MamA, a magnetosome-associated TPR-containing protein, promotes complex assembly. Proc. Natl. Acad. Sci. U.S.A. *108*, E480-E487.

Zeytuni, N., and Zarivach, R. (2012). Structural and functional discussion of the tetra-trico-peptide repeat, a protein interaction module. Structure *20*, 397-405.

Zhang, L., Zhou, Y., Cheng, C., et al. (2015). Genomic analyses reveal mutational signatures and frequently altered genes in esophageal squamous cell carcinoma. Am. J. Hum. Genet. *96*, 597-611.

Zhang, X., Zhang, Q., Xin, Q., et al. (2012). Complex structures of the abscisic acid receptor PYL3/RCAR13 reveal a unique regulatory mechanism. Structure *20*, 780-790.